



Accreting on the Edge: A Luminosity-dependent Cyclotron Line in the Be/X-Ray Binary 2S 1553-542 Accompanied by Accretion Regimes Transition

Malacaria, C.; Bhargava, Y.; Coley, Joel B.; Ducci, L.; Pradhan, P.; Ballhausen, R.; Fuerst, F.; Islam, N.; Jaisawal, G. K.; Jenke, P.

Total number of authors:
18

Published in:
Astrophysical Journal

Link to article, DOI:
[10.3847/1538-4357/ac524f](https://doi.org/10.3847/1538-4357/ac524f)

Publication date:
2022

Document Version
Publisher's PDF, also known as Version of record

[Link back to DTU Orbit](#)

Citation (APA):

Malacaria, C., Bhargava, Y., Coley, J. B., Ducci, L., Pradhan, P., Ballhausen, R., Fuerst, F., Islam, N., Jaisawal, G. K., Jenke, P., Kretschmar, P., Kreykenbohm, I., Pottschmidt, K., Sokolova-Lapa, E., Staubert, R., Wilms, J., Wilson-Hodge, C. A., & Wolff, M. T. (2022). Accreting on the Edge: A Luminosity-dependent Cyclotron Line in the Be/X-Ray Binary 2S 1553-542 Accompanied by Accretion Regimes Transition. *Astrophysical Journal*, 927(2), Article 194. <https://doi.org/10.3847/1538-4357/ac524f>

General rights

Copyright and moral rights for the publications made accessible in the public portal are retained by the authors and/or other copyright owners and it is a condition of accessing publications that users recognise and abide by the legal requirements associated with these rights.

- Users may download and print one copy of any publication from the public portal for the purpose of private study or research.
- You may not further distribute the material or use it for any profit-making activity or commercial gain
- You may freely distribute the URL identifying the publication in the public portal

If you believe that this document breaches copyright please contact us providing details, and we will remove access to the work immediately and investigate your claim.



Accreting on the Edge: A Luminosity-dependent Cyclotron Line in the Be/X-Ray Binary 2S 1553-542 Accompanied by Accretion Regimes Transition

C. Malacaria^{1,2,21} , Y. Bhargava³ , Joel B. Coley^{4,5} , L. Ducci⁶, P. Pradhan⁷ , R. Ballhausen^{8,9}, F. Fuerst¹⁰ , N. Islam^{11,12} , G. K. Jaisawal¹³ , P. Jenke¹⁴, P. Kretschmar¹⁵ , I. Kreykenbohm¹⁶, K. Pottschmidt^{5,17} , E. Sokolova-Lapa^{16,18}, R. Staubert⁶, J. Wilms¹⁶ , C. A. Wilson-Hodge¹⁹ , and Michael T. Wolff²⁰

¹Universities Space Research Association, Science and Technology Institute, 320 Sparkman Drive, Huntsville, AL 35805, USA

²NASA Marshall Space Flight Center, NSSTC, 320 Sparkman Drive, Huntsville, AL 35805, USA

³Inter-University Centre for Astronomy and Astrophysics, Post Box No. 4, Ganeshkhind, Pune-411007 India

⁴Department of Physics and Astronomy, Howard University, Washington, DC 20059, USA

⁵CRESST and Astroparticle Physics Laboratory, NASA Goddard Space Flight Center, Greenbelt, MD 20771, USA

⁶Institut für Astronomie und Astrophysik, Kepler Center for Astro and Particle Physics, Universität Tübingen, Sand 1, D-72076 Tübingen, Germany

⁷Massachusetts Institute of Technology, 77 Massachusetts Avenue, Cambridge, MA 02139, USA

⁸Department of Astronomy, University of Maryland, College Park, MD 20742, USA

⁹NASA-GSFC/CRESST, Astrophysics Science Division, Greenbelt, MD 20771, USA

¹⁰Quasar Science Resources S.L for European Space Agency (ESA), European Space Astronomy Centre (ESAC), Camino Bajo del Castillo s/n, E-28692 Villanueva de la Cañada, Madrid, Spain

¹¹Center for Space Science and Technology, University of Maryland, Baltimore County, 1000 Hilltop Circle, Baltimore, MD 21250, USA

¹²X-ray Astrophysics Laboratory, NASA Goddard Space Flight Center, Greenbelt, MD 20771, USA

¹³National Space Institute, Technical University of Denmark, Elektrovej 327-328, DK-2800 Lyngby, Denmark

¹⁴University of Alabama in Huntsville (UAH), Center for Space Plasma and Aeronomic Research (CSPAR), 301 Sparkman Drive, Huntsville, AL 35899, USA

¹⁵European Space Agency (ESA), European Space Astronomy Centre (ESAC), Camino Bajo del Castillo s/n, E-28692 Villanueva de la Cañada, Madrid, Spain

¹⁶Remis-Observatory and Erlangen Centre for Astroparticle Physics, Friedrich-Alexander-Universität Erlangen-Nürnberg, Sternwartstrasse 7, D-96049 Bamberg, Germany

¹⁷Department of Physics and Center for Space Science and Technology, University of Maryland, Baltimore County, Baltimore, MD 21250, USA

¹⁸Sternberg Astronomical Institute, M.V. Lomonosov Moscow State University, Universitetskij Prospekt, 13, Moscow 119992, Russia

¹⁹ST 12 Astrophysics Branch, NASA Marshall Space Flight Center, Huntsville, AL 35812, USA

²⁰Space Science Division, U.S. Naval Research Laboratory, Washington, DC 20375-5352, USA

Received 2021 December 9; revised 2022 February 4; accepted 2022 February 4; published 2022 March 15

Abstract

Accreting X-ray pulsars undergo luminous X-ray outbursts during which the luminosity-dependent spectral and timing features of the neutron star's emission can be analyzed in detail, thus shedding light on the accretion regime at work. We took advantage of a monitoring campaign that was performed with NuSTAR, Swift/XRT, AstroSat and NICER to follow the Be/X-ray Binary 2S 1553-542 along one of its rare outbursts, and thus trace its spectral and timing evolution. We report the discovery of a luminosity-dependent cyclotron line energy for the first time in this source. The pulse profiles and pulsed fraction also show variability along the outburst, which is consistent with the interpretation that the source transitions from the subcritical to the supercritical accretion regime, separated by a critical luminosity of $L_{\text{crit}} \approx 4 \times 10^{37}$ erg s⁻¹.

Unified Astronomy Thesaurus concepts: Stellar accretion disks (1579); Neutron stars (1108); Magnetic fields (994); X-ray binary stars (1811)

1. Introduction

Accreting X-ray pulsars (XRP) are binary systems where a neutron star (NS) accretes matter supplied by a donor companion star via stellar wind or Roche-lobe overflow. Most XRP pertain to the subclass of Be/X-ray Binaries (BeXRBs), in which the donor companion is a B star whose circumstellar accretion disk shows H α Balmer emission lines.

2S 1553-542 is a BeXRB that was discovered with the SAS-3 observatory (Walter 1976), which also detected pulsations at about 9.3 s several years later (Kelley et al. 1982). Only a few X-ray outbursts have been observed from this source (see Tsygankov et al. 2016, and references therein). The optical companion has been identified as a B1-2V type star

(Lutovinov et al. 2016), and the system lies at a distance of 20 ± 4 kpc (Tsygankov et al. 2016). No Gaia counterpart is found in the Early Data Release 3 (Fabricius et al. 2021) within $\sim 5''$ from the SIMBAD astronomical database (Wenger et al. 2000) source position, nor from the Chandra source position determined by Lutovinov et al. (2016).

As observed by Chandra and Swift/XRT (Lutovinov et al. 2012), and RXTE/PCA (Pahari & Pal 2012), the source average spectrum can fit with a highly absorbed ($N_{\text{H}} \sim 10^{22}$ cm⁻²) cutoff power law that is modified by a blackbody component (kT \sim 2–4 keV) plus an Iron K α emission line at 6.4 keV. Moreover, during the previous outburst observed with NuSTAR in 2015, a Cyclotron Resonant Scattering Feature (CRSF, or cyclotron line) was identified in the spectrum around 25 keV (Tsygankov et al. 2016). A cyclotron line is an important diagnostic of the physics in the X-ray emission region. The energy of the fundamental line, E_{cyc} , probes the magnetic field strength at the site of spectral emission, $E_{\text{cyc}} \sim 11.6 \times B_{12}(1 + z_{\text{g}})^{-1}$ keV, where B_{12} is the magnetic field in units of 10^{12} G, and z_{g} is the gravitational redshift (see Staubert et al. 2019 for a recent review). Moreover,

²¹ NASA Postdoctoral Fellow.

Table 1
Log of the Source Observations Used in this Work

	ObsID	MJD	Exposure
		(Start)	(ks)
Swift/XRT	000310960[08–10]	59233.8	4.3
NuSTAR	90701302002	59236.9	28.3
SXT	9000004204	59268.2	18.8
LAXPC	9000004204	...	37.0
NICER	3202030101	59268.1	1.4

E_{cyc} has been observed to be luminosity dependent in some sources (Staubert et al. 2019). This luminosity dependence appears to be either positive or negative, according to the NS accretion regime. In fact, the dominant physical mechanisms that drive the accretion flow on the NS surface are distinguished according to the so-called critical luminosity, above which a radiation-dominated radiative shock occurs within the accreting structure at the magnetic poles (Davidson & Ostriker 1973; Basko & Sunyaev 1976; Becker et al. 2012; Mushtukov et al. 2015a).

Recently, 2S 1553-542 has undergone a new outburst episode (Nakajima et al. 2019). We consequently initiated a comprehensive observational campaign with NuSTAR, AstroSat and NICER, during which the source was also observed with Swift/XRT. Thanks to this campaign, the source was observed at two different outburst stages—the first near the peak of the outburst, at a luminosity that is about 30% brighter than that observed during the previous outburst, and the second toward the end of the outburst—, thus bracketing the luminosity previously covered by the NuSTAR observation in 2015. Here, we present the results of our study in terms of the spectral and timing characteristics of 2S 1553-542 and we argue that the source has been observed undergoing an accretion regime transition.

2. Data Reduction

A log of all used observations is shown in Table 1, while a light curve of the outburst is shown in Figure 1. Hereafter, we refer to Obs. I as that including Swift/XRT and NuSTAR data, and to Obs. II as that including NICER and AstroSat data, which were taken almost simultaneously. Spectra were rebinned to have at least 50 counts per bin. As advised by the instruments teams, a systematic error of 1% has been applied for all of the spectra from Obs. II. The spectral data were analyzed using XSPEC v12.11.1 c (Arnaud 1996).

2.1. NuSTAR

NuSTAR (Harrison et al. 2013) was launched in 2012. It is currently the only X-ray mission with a telescope that is able to focus hard X-rays up to 79 keV. NuSTAR consists of two identical co-aligned telescopes that focus X-ray photons onto two independent Focal Plane Modules, FPMA and FPMB. At the focus of each telescope module are four (2×2) solid-state cadmium zinc telluride (CdZnTe) imaging detectors. These provide wide-band (3–79 keV) energy coverage with a FWHM of $18''$ and a spectral resolution of 400 eV at 10 keV.

NuSTAR observed 2S 1553-542 on 2021 January 22 (ObsID 90701302002, MJD 59236, Malacaria et al. 2021). The total exposure time was about 28 ks. NuSTAR data were reduced with NUSTARDAS v2.0.0 provided by the HEASOFT v6.28 and using the CALDB 20210202 (Madsen et al. 2020). Cleaned events were obtained following the standard NuSTAR guidelines. Source spectra were extracted through the NUPRODUCTS routine. The source extraction region was a $70''$ radius circular region that was

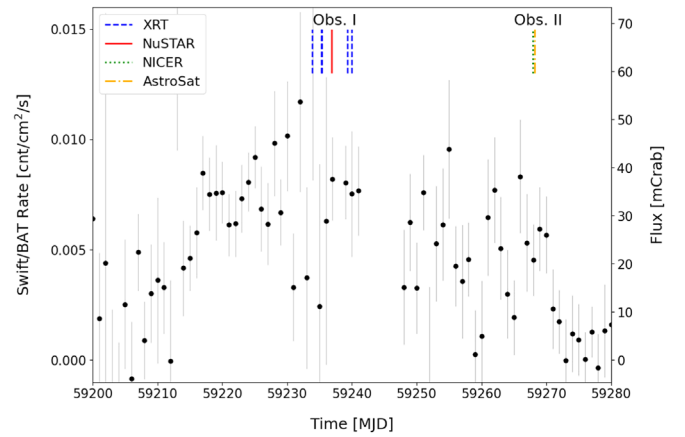


Figure 1. Swift/BAT daily average light curve of 2S 1553-542 during the outburst in 2021 (black dots with gray error bars). The start times of each pointed observation are marked by vertical colored lines as detailed in the legend (same XRT ObsIDs may have slightly different MJDs). Separately analyzed observations (Obs. I and Obs. II) are labeled as detailed in Section 2 and Table 2.

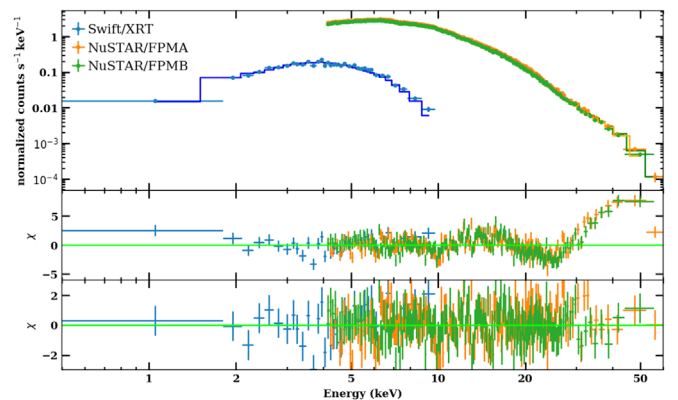


Figure 2. Top: 2S 1553-542 spectrum as observed by Swift/XRT (blue) and NuSTAR (FPMA and FPMB, orange and green, respectively) in 2021 and fitted with a `cutoffpl` model (Table 2, Obs. I). Middle: residuals of the `cutoffpl` model without a Gaussian absorption component. Bottom: residuals of the best-fit `cutoffpl` model including a Gaussian absorption line at ~ 27 keV (see Table 2). Spectra and residuals have been rebinned for plotting purposes.

centered on the source, while the background was extracted from a source-free region of comparable radius on the same detector (Det 0) for FPMA and on the adjacent detector (Det 1) for FPMB. NuSTAR spectral data were used in the range 4–60 keV (background counts dominate the spectrum above 60 keV).

2.2. Swift

The Neil Gehrels Swift Observatory (Gehrels et al. 2004) carries three scientific instruments covering a broad energy range of ~ 0.002 –150 keV: the Burst Alert Telescope (BAT, 15–50 keV), the X-ray Telescope (XRT, 0.5–10 keV), and the UV/Optical Telescope (UVOT, not considered in this work). Swift/BAT performs daily scans of the X-ray sky (Krimm et al. 2013) and the daily light curve of 2S 1553-542 is here adopted from the public BAT transients monitor²² (see Figure 1). On the other hand, Swift/XRT performed pointed observations of 2S 1553-542 during the entire outburst episode

²² <https://swift.gsfc.nasa.gov/results/transients/weak/H1553-542/>

with variable cadence, starting on 2020 January 7 (MJD 59221) through to 2021 March 31 (MJD 59304). However, to ensure similar physical conditions as those sampled by the NuSTAR observation, we only analyzed adjacent Swift/XRT ObsIDs, that is 00031096008 through 00031096010. We verified that the best-fit spectrum of each ObsID was in agreement and then merged the data to improve the statistics.

Swift/XRT data were reduced with XRTDAS v3.6.0, provided by the HEASOFT v6.28 and using the CALDB 20200724. Given the relatively high count rate of the source as detected by XRT ($\sim 1.5 \text{ c s}^{-1}$), we excised the source core using a $13''$ extraction region to avoid pile-up effects. The background was selected from an annular region that was centered on the source. All of the Swift/XRT observations were carried out in PC mode, whose timing resolution is insufficient for a timing analysis of the pulse profile for 2S 1553-542.

2.3. AstroSat

AstroSat is the first Indian multi-wavelength space observatory. It was launched on 2015 September 28, and it carries five scientific instruments onboard (Singh et al. 2014). In this work, we will use data only from the Soft X-ray focusing Telescope (SXT), and the Large Area X-ray Proportional Counter 2 (LAXPC20). Following our Discretionary Director’s Time request (PI: Malacaria), AstroSat observed 2S 1553-542 on 2021 February 23 (ObsID T03_272T01_9000004204).

2.3.1. SXT

The SXT instrument onboard AstroSat is a grazing incidence X-ray telescope that is able to focus X-rays in the 0.3–8 keV nominal energy band, with a thermo-electrically cooled CCD detector in the focal plane. SXT observed 2S 1553-542 in Photon Counting (PC) mode with an exposure of 20 ks. SXT data were processed following the official SXT walkthrough webpage²³ and using the sxtpipeline v1.4b software with the newest available CALDB (20160505). Merged cleaned events were obtained with the SXT Event Merger Tool.²⁴ In a fashion similar to Chaudhury et al. (2018), we verified the optimal extraction region for the source events and selected a circular region with $10'$ radius centered at the source position corrected for the SXT misalignment.²⁵ As suggested by the official SXT instrument team²⁶, the employed background spectrum is the one that is distributed by the Tata Institute of Fundamental Research payload operation centers (TIFR-POC). The Redistribution Matrix File (RMF) that was employed is made available from the SXT official team (sxt_pc_mat_g0to12.rmf, version 2020 June 13), and includes the full grade 0–12 range. Using the sxtARFModule software, the standard SXT Ancillary Response File (ARF) was corrected to account for the observation-specific parameters, such as the area of the source extraction region and vignetting effects. Given the relatively low source count rate ($\sim 2 \text{ cnt s}^{-1}$), no pile-up correction was necessary. Finally, because the SXT data reduction pipeline does not correct for unaccounted gain drifts in the RMF, the gain fit tool in XSPEC was used to calculate the best-fit energy gain offset, while freezing the gain

slope at 1 (Antia et al. 2021). This resulted in a positive gain offset of $0.048 \pm 0.009 \text{ keV}$ —similar to Chaudhury et al. (2018) and Chakraborty et al. (2020)—, which was subsequently applied to the SXT RMF for optimal fitting. Similarly to Bhargava et al. (2019), SXT spectral data are here only considered in the energy band 1–7 keV.

2.3.2. LAXPC

There are in total three identical LAXPC units onboard AstroSat, namely LAXPC10, LAXPC20, and LAXPC30. They are all Xenon+Methane, high-pressure (2 atm) proportional counters, and together they cover an effective area of about 6000 cm^2 in the 5–20 keV energy band. Each LAXPC detects X-ray photons in the energy range 3–80 keV with an energy resolution of 20% at 30 keV (Antia et al. 2021). However, LAXPC30 was switched off in 2018 due to abnormal gain changes, while LAXPC10 is currently working at gain lower than nominal. Therefore, only LAXPC20 data have been used in this work. LAXPC data have been reduced with LAXPC-Software²⁷ (Format A, version 20200804). For optimal S/N ratio, only events from the top layer have been considered. The official AstroSat tools that are released with the data reduction software were used to obtain source and background spectra in the 5–30 keV, as well as source and background light curves, following the method outlined in Misra et al. (2021). Similarly to SXT (see Section 2.3.1), the best-fit energy gain offset has been calculated through the gain fit tool in XSPEC and this resulted in an offset of $-0.52 \pm 0.05 \text{ keV}$ (in agreement with Antia et al. 2021). The background spectrum was also rescaled for the deadtime effect. We also verified that the LAXPC Field of View ($1^\circ \times 1^\circ$) was free from significantly contaminating X-ray sources.

2.4. NICER

NICER (Gendreau & Arzoumanian 2017) is an X-ray telescope deployed on the International Space Station in 2017 June. The NICER X-ray Timing Instrument has 56 aligned Focal Plane Modules (FPMs, 52 currently operational), each made up of an X-ray concentrator optic associated with a silicon drift detector. Together, all of the FPMs result in a peak collecting area of 1900 cm^2 at 1.5 keV. NICER is capable of fast-timing observations in the 0.2–12.0 keV band, with timing accuracy of time-tagged photons to better than 100 ns. (LaMarr et al. 2016; Okajima et al. 2016; Prigozhin et al. 2016; Gendreau & Arzoumanian 2017)

Following our Discretionary Director’s Time proposal, NICER observed 2S 1553-542 in coordination with AstroSat observations on 2021 February 23, for a total exposure time of 1.4 ks (ObsID 3202030101), and successively on February 26 (ObsID 3202030102). However, only data from the former observation have been considered in this work (given its contemporaneity with AstroSat observations). NICER data were processed with HEASOFT version 6.28 and the NICER Data Analysis Software (nicerdas) version 7.0 (2020-04-23V007a) with Calibration Database (CALDB) version xti20200722, adopting standard calibration and screening criteria implied in the nicerl2 tool. The background spectrum was obtained using the space-weather method

²³ http://astrosat-ssc.iucaa.in/uploads/sxt/SXT_walkthrough.pdf

²⁴ https://www.tifr.res.in/~astrosat_sxt/dataanalysis.html

²⁵ http://astrosat-ssc.iucaa.in/uploads/APPS/NoteOnRelativeAngleBetweenPayloads_Astrosat_15072016.pdf

²⁶ https://www.tifr.res.in/~astrosat_sxt/dataanalysis.html

²⁷ <http://astrosat-ssc.iucaa.in/laxpcData>

Table 2

 Best-fit Results of 2S 1553-542 Spectral Analysis with a Cutoff Power-law Model `cutoffpl` Combined with One or Two Blackbody Components, an Iron $K\alpha$ Line and a Cyclotron Line

	Obs I	Obs II
C_{FPMA}	1 (fixed)	...
C_{FPMB}	$1.045^{+0.002}_{-0.002}$...
C_{XRT}	$1.16^{+0.02}_{-0.02}$...
C_{LAXPC}	...	1 (fixed)
C_{NICER}	...	$0.98^{+0.01}_{-0.01}$
C_{SXT}	...	$1.05^{+0.01}_{-0.02}$
$N_{\text{H}} [10^{22} \text{ cm}^{-2}]$	$4.7^{+0.3}_{-0.4}$	$4.1^{+0.2}_{-0.5}$
$kT_{\text{Cold BB}} [\text{keV}]$...	$0.049^{+0.003}_{-0.003}$
$\text{norm}_{\text{Cold BB}}$...	$(1.4^{+3.6}_{-1.2}) \times 10^{11}$
$kT_{\text{HotBB}} [\text{keV}]$	$1.29^{+0.05}_{-0.02}$	$1.68^{+0.07}_{-0.06}$
$\text{norm}_{\text{Hot BB}}$	$10.2^{+1.3}_{-0.9}$	$1.3^{+0.2}_{-0.2}$
$E_{K\alpha} [\text{keV}]$	$6.45^{+0.05}_{-0.04}$...
$\sigma_{K\alpha} [\text{keV}]$	$0.30^{+0.06}_{-0.06}$...
$\text{norm}_{K\alpha} [\text{ph}/\text{cm}^2/\text{s}]$	$(4.4^{+0.7}_{-0.8}) \times 10^{-4}$...
Γ	$-0.7^{+0.3}_{-0.4}$	$0.29^{+0.07}_{-0.06}$
$\text{HighECut} [\text{keV}]$	$5.6^{+0.4}_{-0.5}$	$9.9^{+1.4}_{-0.8}$
$\text{norm}_{\Gamma}^{\text{a}}$	$0.007^{+0.004}_{-0.003}$	$0.013^{+0.001}_{-0.001}$
$E_{\text{cyc}} [\text{keV}]$	$27.2^{+0.3}_{-0.3}$	$22.9^{+0.8}_{-0.6}$
$\sigma_{\text{cyc}} [\text{keV}]$	$6.9^{+0.5}_{-0.5}$	$3.1^{+0.7}_{-0.6}$
$\text{Strength}_{\text{cyc}} [\text{keV}]$	$11.2^{+2.2}_{-1.6}$	$2.3^{+1.3}_{-0.7}$
$\text{Flux}^{\text{b}} (3\text{--}30 \text{ keV})$	$1.481^{+0.003}_{-0.003} \times 10^{-9}$	$7.34^{+0.03}_{-0.03} \times 10^{-10}$
$\text{Flux}^{\text{b}} (3\text{--}20 \text{ keV})$	$1.321^{+0.002}_{-0.002} \times 10^{-9}$	$6.09^{+0.03}_{-0.03} \times 10^{-10}$
$\chi^2/\text{d.o.f.}$	1338/1223	887/791

Notes. All of the reported errors are at 1σ c.l., obtained using the `err` tool from XSPEC.

^a In units of photons/keV/cm²/s at 1 keV.

^b Flux calculated for the entire model and reported in units of erg cm⁻² s⁻¹. Flux values with estimated errors were obtained using the `cflux` model from XSPEC as resulting from FPMA and LAXPC in Obs. I and II, respectively.

implemented in the version `v0p6` of the `nicer_bkg_estimator`²⁸ tool (K. Gendreau et al., 2022, in preparation). The energy band of NICER spectrum was limited to 0.75–9 keV, below which the spectrum was background dominated and to avoid potential noise at the high-energy end of the bandpass.

3. Results

3.1. Spectral Analysis

To compare our results with those available from Tsygankov et al. (2016), we adopted a similar spectral model; that is, an absorbed cutoff power-law model (`cutoffpl` in XSPEC) that is modified with a soft blackbody (`bbbodyrad`), a Fe $K\alpha$ emission line (`Gauss`) at 6.4 keV, and an absorption line with Gaussian optical depth profile (`gabs`) to take into account the CRSF. Different continuum components (`Highcut`, `CompTT`) were tested in place of the cutoff power-law component and they all require a cyclotron line to fit the data. The photoelectric absorption component `tbabs` from XSPEC was used assuming model-relative (`wilm`) elemental abundances (Wilms et al. 2000). Moreover, because the Obs. II is carried out at a luminosity level that is lower than that analyzed

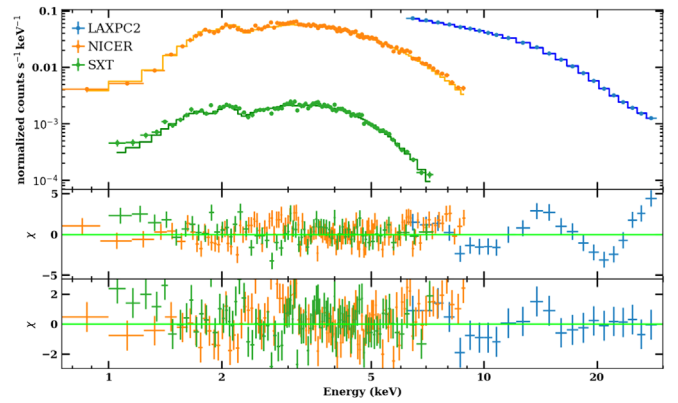


Figure 3. Top: 2S 1553-542 spectrum as observed by NICER (orange) and AstroSat (SXT and LAXPC2, green and blue, respectively) in 2021 and fitted with a `cutoffpl` model (Table 2, Obs. II). Middle: residuals of the `cutoffpl` model without a Gaussian absorption component. Bottom: residuals of the best-fit `cutoffpl` model including a Gaussian absorption line at ~ 23 keV (see Table 2). Spectra and residuals have been rebinned for plotting purposes.

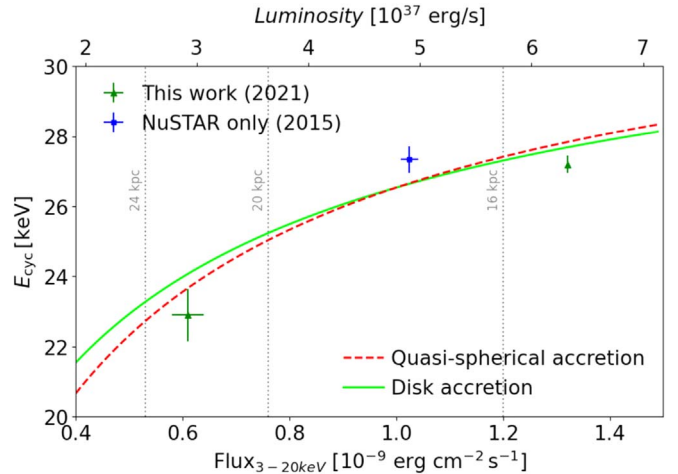


Figure 4. Cyclotron line energy E_{cyc} as a function of flux (bottom x axis) and luminosity (top x axis, $d = 20$ kpc) in the 3–20 keV energy range. Error bars indicate the 1σ c.l. The lime-continuous line and the red-dashed line show a fit to the data points with the collisionless shock model (see Section 4.1) for the disk accretion and the quasi-spherical settling accretion, respectively. Gray vertical lines show the critical luminosity L_{crit} (from Equation (1)) obtained from the bottom x axis fluxes for different distance values ($d = 20 \pm 4$ kpc).

in Tsygankov et al. (2016), a few additional measures need to be taken. In particular, the spectrum obtained from Obs. II does not require a Fe $K\alpha$ emission line but it does require a second, colder blackbody component.

A cross-normalization constant was applied to take into account uncertainties in calibration among the various instruments. The seemingly large cross-normalization value between Swift/XRT and NuSTAR, $\sim 16\%$, is in fact consistent with the expected range from Madsen et al. (2015) and others (see, e.g., Molina et al. 2019), and also reflects the intrinsic source variability between observations (see Figure 1).

Our spectral analysis from two different outburst stages is presented in Table 2. Obs I and Obs II spectra are shown in Figure 3 and Figure 4, respectively. Spectral results show a variation of the cyclotron line energy with luminosity (see Figure 4). A comparison of our results with those obtained from

²⁸ https://heasarc.gsfc.nasa.gov/docs/nicer/tools/nicer_bkg_est_tools.html

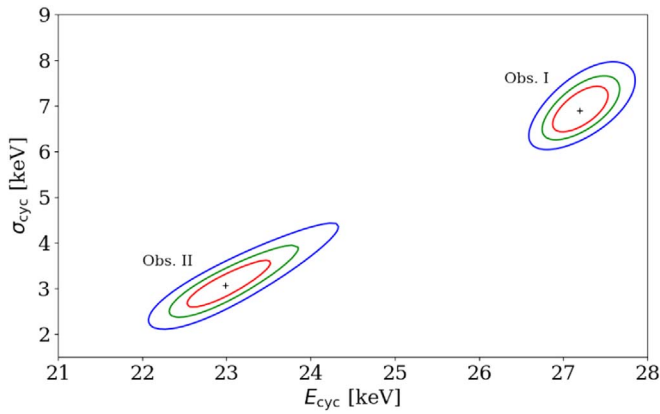


Figure 5. χ^2 -contour plots for two parameters, E_{cyc} and σ_{cyc} from Obs. I and II, as indicated. Red, green and blue contours correspond to the 68%-uncertainty for one and two parameters of interest, and to the 90%-uncertainty for two parameters of interest, respectively. The black cross in the midst of the contours indicates the best-fit solution.

the NuSTAR observation of 2S 1553-542 in 2015 (Tsygankov et al. 2016, Model II solution in their work) is also shown in Figure 4. For reference, the best-fit Model II in Tsygankov et al. (2016) shows a spectral photon index $\Gamma = -0.66$, a cutoff energy $E_{\text{cut}} = 5.1$ keV, a blackbody component with $kT_{\text{BB}} = 0.94$ and $\text{norm}_{\text{BB}} \simeq 20$, an Iron $K\alpha$ line at 6.45 keV and $\sigma_{K\alpha} = 0.4$ keV, and a cyclotron line with $E_{\text{cyc}} = 27.3$ keV, $\sigma_{\text{cyc}} = 6.4$ keV, $\tau_{\text{cyc}} = 8.3$ keV. We also notice that, similarly to Tsygankov et al. (2016), an uncommonly hard photon index was obtained for the Obs. I spectrum (see Table 2), in opposition with the Obs. II spectral photon index. We therefore verified that the best-fit solution did not result from the lack of a cold blackbody component in Obs. I that, given the large emitting radius, may represent the emerging radiation from the accretion disk becoming relevant as the main source continuum becomes fainter. Restricting the photon index to positive values only and adding a cold blackbody component (best-fit values $kT_{\text{Cold BB}} \sim 0.18$, $\text{norm}_{\text{Cold BB}} \sim 2.8E4$) results in a slightly worse $\chi^2/d.o.f. = 1346/1221$. In this case, other model parameters remain roughly consistent with those reported in Table 2, with the largest difference (i.e., $\sim 40\%$) shown by the normalization of the hot blackbody component, $\text{norm}_{\text{Hot BB}} = 7.3_{-0.9}^{+1.2}$, while the best-fit value of the photon index, $\Gamma = 0.0_{-0.0}^{+0.4}$, gets pegged at its lower limit. Even in the case where the photon index $\Gamma \geq 0$ and a cold blackbody component is included, the Obs. I best-fit model returns a value of the cyclotron line energy that remains almost unchanged, $E_{\text{cyc}} = 27.1_{-0.3}^{+0.3}$ keV.

To rule out possible artificial (model-driven) dependencies of the cyclotron line energy E_{cyc} and other model parameters, we analyzed the correspondent χ^2 -contour plots. No significant dependence of the E_{cyc} on any continuum parameters was found, but the CRSF Gaussian parameters were found to be correlated. However, confidence level contour plots clearly show separated intervals, thus supporting the physical interpretation of the cyclotron line energy luminosity dependence. This is shown, for example, in Figure 5 for E_{cyc} versus σ_{cyc} (with a similar behavior for E_{cyc} versus $\text{Strength}_{\text{cyc}}$ contour plots).

3.2. Timing Analysis

To more thoroughly investigate possible changes in the accretion regime during our observations, we extracted

energy-dependent pulse profiles from the source at different luminosities. To do so, we applied the following corrections.

For NuSTAR, source and background light curves were extracted with a 0.1 s bin size using the `nuproducts` tool. NuSTAR light curves were barycentered using the `barycorr` tool and the NuSTAR clock correction file `nuClock20100101v118`. LAXPC20 light curves also were extracted with a 0.05 s bin size and barycentered using the online orbit file generator²⁹ and the official AstroSat tools for Header keywords correction `prepary_laxpc` and for Barycentric correction `asbary`.³⁰ The same corrections (except the background subtraction) were applied to the NICER light curve. Orbital demodulation was also applied to all datasets, based on the recently updated orbital solution from Malacaria et al. (2020). Pulse periods were obtained from the NuSTAR FPMA and FPMB combined, background-corrected light curves for Obs. I, and from AstroSat/LAXPC20 background-corrected light curves for Obs. II. Pulse periods were determined using the epoch folding technique (Leahy et al. 1983) through the `efsearch` HEASARC tool. The process results in a pulse period value of 9.282155(3) s for Obs. I and 9.279490(8) for Obs. II. The spin period derivative is therefore $\dot{P}_s = -9.8 \times 10^{-10} \text{ s s}^{-1}$ ($\dot{\nu} = 1.1 \times 10^{-11} \text{ Hz s}^{-1}$). Pulse periods uncertainties were estimated by simulating light curves from the previously determined pulse profiles, following the method outlined in Lutovinov et al. (2012) and Boldin et al. (2013). 10^3 light curves were simulated, with count rates generated randomly within the error of the original data. Epoch folding was then applied to each simulated light curve to obtain a pulse periods distribution. The standard deviation of such distribution was taken as the pulse period uncertainty of the data.

To allow a comparison with the pulse profiles obtained by Tsygankov et al. (2016), we extracted pulse profiles in the same energy bands (i.e., 3–7, 7–18, and 18–30 keV) for our NuSTAR and AstroSat/LAXPC observations. The NICER pulse profile in the 1–3 keV energy band was also extracted. The energy- and luminosity-resolved pulse profiles are shown in Figure 6. Due to the non-monotonic variation of the pulse period throughout the outburst and to the residual wave-like behavior of the spin frequency evolution around the best orbital solution seen in Fermi/GBM³¹, the pulse profiles at different times are not phase connected. Therefore, in Figure 6 they have been manually aligned with respect to the peak of the NuSTAR pulse profile in the 7–18 keV energy band.

4. Discussion

4.1. Spectral Analysis

A luminosity dependence of the parameters characterizing the XRP's spectral model is observed in many sources and is expected from theoretical arguments (see, e.g., Staubert et al. 2019, and references therein). According to the theoretical models (Basko & Sunyaev 1976; Becker et al. 2012; Poutanen et al. 2013; Mushtukov et al. 2015a, 2015b), two different accretion regimes are at work in the accretion structure, depending on the accretion rate and therefore luminosity. These two different accretion regimes are separated by a critical

²⁹ <http://astrosat-ssc.iucaa.in:8080/orbitgen/>

³⁰ http://astrosat-ssc.iucaa.in/data_and_analysis

³¹ <https://gamma-ray.nsstc.nasa.gov/gbm/science/pulsars/lightcurves/2s1553.html>

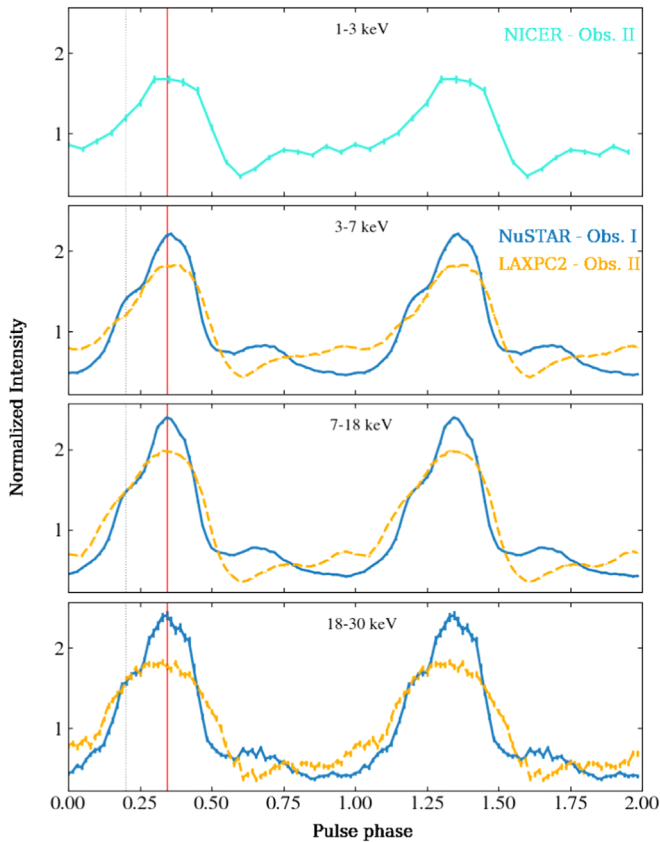


Figure 6. Energy- and luminosity-resolved pulse profiles of 2S 1553-542 as observed during the outburst in 2021 with NICER (top panel), NuSTAR and AstroSat (remaining panels) in the energy bands 1–3, 3–7, 7–18, 18–30 keV from top to bottom. Pulse profiles are normalized by the average source intensity in each band. The vertical red line marks the main peak in the NuSTAR (7–18 keV) pulse profile, with respect to which the other pulse profiles have been aligned. The gray dotted line at $\phi \sim 0.2$ marks the energy-dependent wing.

luminosity, L_{crit} , which is characterized by a radiation pressure that is so intense that it prevents the accreting matter from freefalling onto the NS surface. This gives rise to a radiative shock and the formation of an accretion column. For a value of the cyclotron line energy of $E_{\text{cyc}} = 27$ keV, the critical luminosity obtained by Becker et al. (2012 see their Equation (55)) is:

$$L_{\text{crit}}^a = 1.28 \times 10^{37} \text{ erg s}^{-1} \left(\frac{\Lambda}{0.1} \right)^{-7/5} \left(\frac{M_{\text{NS}}}{1.4 M_{\odot}} \right)^{29/30} \times \left(\frac{R_{\text{NS}}}{10 \text{ km}} \right)^{1/10} \left(\frac{E_{\text{cyc}}}{10 \text{ keV}} \right)^{16/15} \quad (1)$$

and it is equal to $3.7 \times 10^{37} \text{ erg s}^{-1}$ for $\Lambda = 0.1$ the accretion flow geometry constant for disk accretion, $M_{\text{NS}} = 1.4 M_{\odot}$ the mass of the NS, $R_{\text{NS}} = 12$ km the radius of the NS. Meanwhile, for the same cyclotron line energy Mushtukov et al. (2015a) predicts a critical luminosity value $L_{\text{crit}}^b \sim 1 \times 10^{37} \text{ erg s}^{-1}$ (see, e.g., their Figure 7 for the case of pure X-mode polarization). L_{crit}^a has been shown in Figure 4 for the upper, nominal, and lower values of the source distance, $d = 20 \pm 4$ kpc.

From an observational perspective (see, e.g., Klochov et al. 2011, and references therein), some accreting XRP exhibit a

positive correlation between the E_{cyc} and luminosity when the source is accreting in the subcritical ($L < L_{\text{crit}}$) regime, while a few accreting XRPs show the opposite correlation in the supercritical ($L > L_{\text{crit}}$) regime. In contrast, some sources do not show any correlation (e.g., 4U 1538-522, Hemphill et al. 2016), while a few sources show either both correlations (V 0332+53, Doroshenko et al. 2017, and GRO J1008-57, Chen et al. 2021) or a flattening of the parameters dependence (Rothschild et al. 2017; Vybornov et al. 2017). For V 0332+53, the reported inversion of the cyclotron line energy luminosity dependence has been interpreted as evidence for accretion regime transition. An analogous interpretation was suggested for GRO J1008-57 based on the continuum spectral evolution solely, but is not yet supported by the pulse profile behavior (Kühnel et al. 2013).

Even though only a handful of data points are available in Figure 4, the trend suggests a positive correlation of E_{cyc} with luminosity and perhaps following flattening, similar to what has been observed in GX 304-1 (Rothschild et al. 2017) and Cep X-4 (Vybornov et al. 2017). However, the flattening in those two sources was observed at a subcritical accretion regime, where the accretion flow possibly decelerates in a collisionless shock (Langer & Rappaport 1982) that only exists when the accretion rate is low (i.e., a few percent of the Eddington luminosity, Braun & Yahel 1984; Bykov & Krasil'Shchikov 2004). For a typical NS mass $M_{\text{NS}} = 1.4 M_{\odot}$, the Eddington luminosity is $L_{\text{Edd}} = 1.3 \times 10^{38} \text{ erg s}^{-1}$, which is about 50% larger than the highest observed luminosity value for 2S 1553-542 in this work. Therefore, the collisionless shock should not play a dominant role at the accretion rates probed in this work, and the cyclotron line energy dependence on luminosity is not expected to flatten similarly to GX 304-1 and Cep X-4. Nonetheless, given the trend observed in Figure 4, we tested the collisionless shock model by fitting the following function (see Equation (6) from Rothschild et al. 2017):

$$E_{\text{cyc}}(F_x) = E_0 (K_1 F_x^{-\alpha} + 1)^{-3} \quad (2)$$

where E_0 is the cyclotron line energy resulting from the NS surface, $K_1 = H_{\text{CRSF}}/R_{\text{NS}}$ (with H_{CRSF} being the height within the accretion structure where the cyclotron line is formed) is assumed constant, F_x is the observed X-ray flux, and $\alpha = 5/7$ for disk accretion. The fit returns $E_0 = 33.8 \pm 1.7$ keV and $K_1 = 0.08 \pm 0.01 (10^{-9} \text{ erg cm}^{-2} \text{ s}^{-1})^{\alpha}$. A similar fit and best-fit values are obtained if $\alpha = 9/11$ for quasi-spherical settling accretion is assumed. These values are comparable to those obtained for GX 304-1 and Cep X-4 (Rothschild et al. 2017; Vybornov et al. 2017).

The trend in Figure 4 may also be interpreted as indicative of an accretion regime transition around the L_{crit} . The critical luminosity values shown in Figure 4 are derived from the observed flux assuming isotropic emission and their maximum uncertainty is estimated as 25% (see Martínez-Núñez et al. 2017). In this interpretation, E_{cyc} correlates with luminosity until L_{crit} is reached, and then either flattens or decreases with luminosity. In this scenario, the distance value plays a key role. In fact, this scenario favors distance values < 20 kpc, with the accretion regime transition occurring at $L_{\text{crit}} \approx 4 \times 10^{37} \text{ erg s}^{-1}$ obtained from Equation (1), corresponding to about 16 kpc in Figure 4. Further analysis of the pulse profiles and of the pulsed fraction support this interpretation (see Section 4.2).

4.2. Timing Analysis

Comparing the luminosity dependence of the pulse profiles at different energy bands can provide insights into the accretion regime at work on the NS. Tsygankov et al. (2016) showed that the pulse profile of 2S 1553-542 is only moderately energy-dependent, with a main broad peak spanning roughly half pulse cycle plus a trailing hard-energy wing that contributes to the main peak and which only shows up in the 18–30 keV energy band (i.e., the energy band sampling cyclotron line). A similar trailing wing was observed in other sources as well (Tsygankov et al. 2006; Iyer et al. 2015). Its interpretation is that of a phase-lagging feature around the cyclotron line energy, which is due to the energy-dependent beaming of the radiation at the site of emission. The emission around the cyclotron line energy escapes through a pencil beam, while the remaining spectrum is mostly emitted in a fan beam fashion (Ferrigno et al. 2011; Schönherr et al. 2014).

The pulse profiles from our monitoring campaign (see Figure 6) show a similarly moderate energy dependence as Tsygankov et al. (2016), with the exception that the hard-energy wing is present at all energy bands that were probed with our NuSTAR observation (carried out at a source luminosity that is about 30% higher). The hard-energy wing only shows energy dependence at the lower luminosity level of the AstroSat observation (Obs. II). Moreover, the AstroSat pulse profiles morphology so strongly resembles that of the pulse profiles obtained with NuSTAR by Tsygankov et al. (2016) that they can be considered as representative of the same accretion regime. In addition, a comparison of the luminosity-dependent profiles that were obtained in this work suggests a narrow beaming component emerging at higher luminosity (the main NuSTAR peak at pulse phase $\phi \sim 0.35$ in Figure 6). The NuSTAR profiles also show a secondary peak that is located around the main minimum of the AstroSat/LAXPC profiles ($\phi \sim 0.65$). Finally, the NICER pulse profile resembles those from AstroSat/LAXPC. This is coherent with the finding that pulse profiles from this source show only moderate energy dependence but, at the same time, a rather marked luminosity dependence, which is consistent with an accretion regime transition once the critical luminosity $L_{\text{crit}} \approx 4 \times 10^{37}$ erg s⁻¹ is crossed.

To study the pulsed fraction (PF), we define it as $(I_{\text{max}} - I_{\text{min}})/(I_{\text{max}} + I_{\text{min}})$, where I_{max} , I_{min} are the maximum and minimum pulse profile count rate, respectively. The PF is high (>50%) and shows a marked luminosity and energy dependence (see Figure 7). At higher luminosity (i.e., that covered by the NuSTAR observation), the pulsed fraction keeps increasing with energy. However, at lower luminosity (i.e., that covered by the AstroSat observation), the pulsed fraction shows a reversal trend around the cyclotron line energy, which is almost identical to that observed by Tsygankov et al. (2016). This strengthens the interpretation that both observations are representative of the same, subcritical accretion regime. Local features around the cyclotron line energy in the energy-dependent pulsed fractions have also been observed in other sources (see, e.g., Ferrigno et al. 2009) and are usually ascribed to the resonant scattering that causes beamed emission to become isotropic. Moreover, the stark difference in trend and value of the pulsed fraction in the 18–30 keV energy band seems to reflect the luminosity dependence of the hard-energy wing that is observed in the pulse profiles.

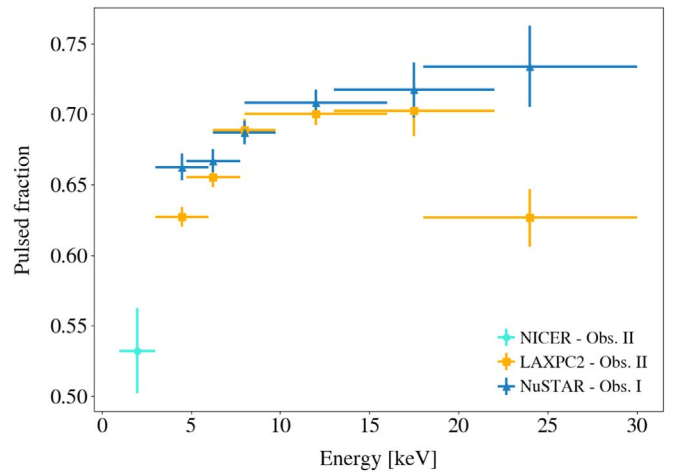


Figure 7. Pulsed fraction plotted as a function of the energy for the pulse profiles shown in Figure 6, subdivided in not independent energy-bins for better visualization. Cyan circles, blue triangles and orange squares data points correspond to NICER, NuSTAR and AstroSat pulse profiles, respectively.

Both the pulse profile and the pulsed fraction luminosity dependence are generally attributed to the switch of the accretion column dominant beaming pattern—the pencil beam dominates at lower luminosity and a fan beam makes a growing contribution as the luminosity increases, with some hybrid configurations in between (see, e.g., Basko & Sunyaev 1975, 1976; Blum & Kraus 2000; Becker et al. 2012, for theoretical models and, e.g., Malacaria et al. 2015; Epili et al. 2017; Wilson-Hodge et al. 2018 for observational results). In this scenario, the pulsed fraction switch in the 18–30 keV energy band proves additional evidence that the accretion regime has drastically changed as the luminosity increased and has eventually crossed the critical luminosity value that was derived in Section 4.1, $L_{\text{crit}} \approx 4 \times 10^{37}$ erg s⁻¹.

5. Summary and Conclusions

We have analyzed the most recent outburst from the accreting XRP 2S 1553-542 at the beginning of 2021, taking advantage of a multi-observatory campaign. We performed spectral and timing analysis, and focused on the spectral and pulse profiles luminosity dependence.

The spectral analysis reveals a positive correlation between the cyclotron line energy and the observed luminosity (Figures 4, 5), which was observed for the first time in this source. The correlation ceases above a certain luminosity, which can be interpreted either in terms of a collisionless shock or as an inversion of the correlation above the critical luminosity L_{crit} . The latter scenario is favored by additional evidence and supports a distance value for 2S 1553-542 of about 16 kpc, which is skewed toward the lower limit of the nominal distance value for this source.

The pulse profile analysis also reveals a drastic change in the pulse profile shape once the source crosses the critical luminosity (Figure 6). This result is supported by a trend inversion of the pulsed fraction corresponding to these profiles, in an energy band that samples the cyclotron line (Figure 7).

Based on these indications, we conclude that we have witnessed an accretion regime transition, which happens at a $L_{\text{crit}} \approx 4 \times 10^{37}$ erg s⁻¹. Given the elusive nature of this phenomenon, the accretion regime transition has rarely been observed. This makes 2S 1553-542 a key addition to the short list of XRPs whose accretion regime transition is supported by

the luminosity dependence of the cyclotron line energy, the pulse profiles, and the pulsed fraction altogether.

This research has made use of data and software provided by the High Energy Astrophysics Science Archive Research Center (HEASARC), which is a service of the Astrophysics Science Division at NASA/GSFC and the High Energy Astrophysics Division of the Smithsonian Astrophysical Observatory. We acknowledge extensive use of the NASA Abstract Database Service (ADS). The material is based upon work supported by NASA under award number 80GSFC21M0002 (CRESST II). This work used data from the NuSTAR mission, which is a project that is led by the California Institute of Technology, managed by the Jet Propulsion Laboratory, and funded by NASA, and has utilized the NUSTARDAS software package, jointly developed by the ASI Science Data Center, Italy, and the California Institute of Technology, USA. This work made use of data supplied by the UK Swift Science Data Centre at the University of Leicester and has also made use of the XRT Data Analysis Software (XRTDAS) developed under the responsibility of the ASI Science Data Center, Italy. This work was supported by NASA through the NICER mission and the Astrophysics Explorers Program. This work has been performed utilizing the calibration data-bases and auxiliary analysis tools developed, maintained and distributed by AstroSat-SXT and LAXPC teams with members from various institutions in India and abroad. C.M. is supported by an appointment with the Universities Space Research Association. E.S.L. acknowledges the support by DFG grant 1830Wi1860/11-1. M.T.W. is supported at NRL by NASA under Interagency Agreement NNG200808A. RB acknowledges support by NASA under award number 80GSFC21M0002.

ORCID iDs

C. Malacaria  <https://orcid.org/0000-0002-0380-0041>
 Y. Bhargava  <https://orcid.org/0000-0002-5967-8399>
 Joel B. Coley  <https://orcid.org/0000-0001-7532-8359>
 P. Pradhan  <https://orcid.org/0000-0002-1131-3059>
 F. Fuerst  <https://orcid.org/0000-0003-0388-0560>
 N. Islam  <https://orcid.org/0000-0002-2413-9301>
 G. K. Jaisawal  <https://orcid.org/0000-0002-6789-2723>
 P. Kretschmar  <https://orcid.org/0000-0001-9840-2048>
 K. Pottschmidt  <https://orcid.org/0000-0002-4656-6881>
 J. Wilms  <https://orcid.org/0000-0003-2065-5410>
 C. A. Wilson-Hodge  <https://orcid.org/0000-0002-8585-0084>
 Michael T. Wolff  <https://orcid.org/0000-0002-4013-5650>

References

Antia, H. M., Agrawal, P. C., Dedhia, D., et al. 2021, *JApA*, 42, 32
 Arnaud, K. A. 1996, in ASP Conf. Ser. 101, *Astronomical Data Analysis Software and Systems V*, ed. G. H. Jacoby & J. Barnes (San Francisco, CA: ASP), 17
 Basko, M. M., & Sunyaev, R. A. 1975, *A&A*, 42, 311
 Basko, M. M., & Sunyaev, R. A. 1976, *MNRAS*, 175, 395
 Becker, P. A., Klochkov, D., Schönherr, G., et al. 2012, *A&A*, 544, A123
 Bhargava, Y., Belloni, T., Bhattacharya, D., & Misra, R. 2019, *MNRAS*, 488, 720

Blum, S., & Kraus, U. 2000, *ApJ*, 529, 968
 Boldin, P. A., Tsygankov, S. S., & Lutovinov, A. A. 2013, *AstL*, 39, 375
 Braun, A., & Yabel, R. Z. 1984, *ApJ*, 278, 349
 Bykov, A. M., & Krasil'Shchikov, A. M. 2004, *AstL*, 30, 309
 Chakraborty, S., Navale, N., Ratheesh, A., & Bhattacharyya, S. 2020, *MNRAS*, 498, 5873
 Chaudhury, K., Chitnis, V. R., Rao, A. R., et al. 2018, *MNRAS*, 478, 4830
 Chen, X., Wang, W., Tang, Y. M., et al. 2021, *ApJ*, 919, 33
 Davidson, K., & Ostriker, J. P. 1973, *ApJ*, 179, 585
 Doroshenko, V., Tsygankov, S. S., Mushtukov, A. A., et al. 2017, *MNRAS*, 466, 2143
 Epili, P., Naik, S., Jaisawal, G. K., & Gupta, S. 2017, *MNRAS*, 472, 3455
 Fabricius, K., Luri, X., Arenou, F., et al. 2021, *A&A*, 649, A5
 Ferrigno, C., Becker, P. A., Segreto, A., Mineo, T., & Santangelo, A. 2009, *A&A*, 498, 825
 Ferrigno, C., Falanga, M., Bozzo, E., et al. 2011, *A&A*, 532, A76
 Gehrels, N., Chincarini, G., Giommi, P., et al. 2004, *ApJ*, 611, 1005
 Gendreau, K., & Arzoumanian, Z. 2017, *NatAs*, 1, 895
 Harrison, F. A., Craig, W. W., Christensen, F. E., et al. 2013, *ApJ*, 770, 103
 Hemphill, P. B., Rothschild, R. E., Fürst, F., et al. 2016, *MNRAS*, 458, 2745
 Iyer, N., Mukherjee, D., Dewangan, G. C., Bhattacharya, D., & Seetha, S. 2015, *MNRAS*, 454, 741
 Kelley, R. L., Ayasli, S., & Rappaport, S. 1982, *IAU Circ.*, 3667, 3
 Klochkov, D., Staubert, R., Santangelo, A., Rothschild, R. E., & Ferrigno, C. 2011, *A&A*, 532, A126
 Krimm, H. A., Holland, S. T., Corbet, R. H. D., et al. 2013, *ApJS*, 209, 14
 Kühnel, M., Müller, S., Kreykenbohm, I., et al. 2013, *A&A*, 555, A95
 LaMarr, B., Prigozhin, G., Remillard, R., et al. 2016, *Proc. SPIE*, 9905, 99054W
 Langer, S. H., & Rappaport, S. 1982, *ApJ*, 257, 733
 Leahy, D. A., Darbro, W., Elsner, R. F., et al. 1983, *ApJ*, 266, 160
 Lutovinov, A., Tsygankov, S., & Chernyakova, M. 2012, *MNRAS*, 423, 1978
 Lutovinov, A. A., Buckley, D. A. H., Townsend, L. J., Tsygankov, S. S., & Kennea, J. 2016, *MNRAS*, 462, 3823
 Madsen, K. K., Grefenstette, B. W., Pike, S., et al. 2020, arXiv:2005.00569
 Madsen, K. K., Harrison, F. A., Markwardt, C. B., et al. 2015, *ApJS*, 220, 8
 Malacaria, C., Jenke, P., Roberts, O. J., et al. 2020, *ApJ*, 896, 90
 Malacaria, C., Klochkov, D., Santangelo, A., & Staubert, R. 2015, *A&A*, 581, A121
 Malacaria, C., Pottschmidt, K., Fuerst, F., et al. 2021, *ATel*, 14348, 1
 Martínez-Núñez, S., Kretschmar, P., Bozzo, E., et al. 2017, *SSRv*, 212, 59
 Misra, R., Roy, J., & Yadav, J. S. 2021, *JApA*, 42, 55
 Molina, M., Malizia, A., Bassani, L., et al. 2019, *MNRAS*, 484, 2735
 Mushtukov, A. A., Suleimanov, V. F., Tsygankov, S. S., & Poutanen, J. 2015a, *MNRAS*, 447, 1847
 Mushtukov, A. A., Tsygankov, S. S., Serber, A. V., Suleimanov, V. F., & Poutanen, J. 2015b, *MNRAS*, 454, 2714
 Nakajima, M., Negoro, H., Kurogi, K., et al. 2019, *ATel*, 13217, 1
 Okajima, T., Soong, Y., Balsamo, E. R., et al. 2016, *Proc. SPIE*, 9905, 1495
 Pahari, M., & Pal, S. 2012, *MNRAS*, 423, 3352
 Poutanen, J., Mushtukov, A. A., Suleimanov, V. F., et al. 2013, *ApJ*, 777, 115
 Prigozhin, G., Gendreau, K., Doty, J. P., et al. 2016, *Proc. SPIE*, 9905, 447
 Rothschild, R. E., Kühnel, M., Pottschmidt, K., et al. 2017, *MNRAS*, 466, 2752
 Schönherr, G., Schwarm, F. W., Falkner, S., et al. 2014, *A&A*, 564, L8
 Singh, K. P., Tandon, S. N., Agrawal, P. C., et al. 2014, *Proc. SPIE*, 9144, 91441S
 Staubert, R., Trümper, J., Kendziorra, E., et al. 2019, *A&A*, 622, A61
 Tsygankov, S. S., Lutovinov, A. A., Churazov, E. M., & Sunyaev, R. A. 2006, *MNRAS*, 371, 19
 Tsygankov, S. S., Lutovinov, A. A., Krivonos, R. A., et al. 2016, *MNRAS*, 457, 258
 Vybornov, V., Klochkov, D., Gornostaev, M., et al. 2017, *A&A*, 601, A126
 Walter, F. 1976, *IAU Circ.*, 2959, 2
 Wenger, M., Ohsenbein, F., Egret, D., et al. 2000, *A&AS*, 143, 9
 Wilms, J., Allen, A., & McCray, R. 2000, *ApJ*, 542, 914
 Wilson-Hodge, C. A., Malacaria, C., Jenke, P. A., et al. 2018, *ApJ*, 863, 9